Soft Matter

Curvature-Controlled Geometric Lensing Behavior in Self-Propelled Colloidal Particle Systems

Journal:	*Soft Matter*
Manuscript ID	SM-ART-07-2022-001012.R1
Article Type:	Paper
Date Submitted by the Author:	09-Sep-2022
Complete List of Authors:	Schoenhoefer, Philipp; University of Michigan, Chemical Engineering Glotzer, Sharon; University of Michigan, Chemical Engineering

Curvature-Controlled Geometrical Lensing Behavior in Self-Propelled Colloidal Particle Systems

Philipp W. A. Schönhöfer[1] and Sharon C. Glotzer[1,2,*]

[1] Department of Chemical Engineering, University of Michigan, Ann Arbor, MI 48109, USA

[2] Biointerfaces Institute, University of Michigan, Ann Arbor, MI 48109, USA

E-mail: sglotzerkjc@umich.edu

Abstract. In many biological systems, the curvature of the surfaces cells live on influence their collective properties. Curvature should likewise influence the behavior of active colloidal particles. We show using molecular simulation of self-propelled active particles on surfaces of Gaussian curvature (both positive and negative) how curvature sign and magnitude can alter the system's collective behavior. Curvature acts as a geometrical lens and shifts the critical density of motility-induced phase separation (MIPS) to lower values for positive curvature and higher values for negative curvature, which we explain theoretically by the nature of parallel lines in spherical and hyperbolic space. Curvature also fluidizes dense MIPS clusters due to the emergence of defect patterns disrupting the crystalline order inside the clusters. Using our findings, we engineer three confining surfaces that strategically combine regions of different curvature to produce a host of novel dynamical behaviors, including cyclic MIPS on sphercylinders, directionally biased cyclic MIPS on spherocones, and position dependent cluster fluctuations on metaballs.

1. Introduction

Mimicry of biological systems has long been a goal in colloidal science. Apart from self-assembly, recreating the dynamics of collective systems – like the swarming of animals [1, 2, 3], the collaborative swimming of bacteria [4, 5] or the dynamics of cell tissue [6] – has received great interest in the last decades. A variety of techniques have been developed to synthesize active colloids [7, 8, 9, 10, 11] that harness internal energy and convert it into a self-propelling force, driving the system perpetually far from equilibrium and into novel phases reminiscent of the behavior of their biological counterparts [12, 13, 14]. For instance, self-propelled colloidal particles (SPPs) interacting only via excluded volume exhibit motility-induced phase separation (MIPS) into dense but mobile crystalline clusters coexisting with a low-density gas above a critical packing fraction [15, 16]. MIPS has been studied predominantly in three [17] or (flat) two dimensions [15]. However, many active organisms live on complex surfaces whose curvature can affect the collective dynamics. In biology, this relationship between activity and surface curvature is illustrated by the collective flow of embryonic tissue during gastrulation

[18] or the migration of epithelial tissue in the gut [19]. Moreover, coherent motile cells are predicted to self-organize into various dynamic patterns based on their geometrical constraints [20]. Although first steps towards studying active colloids on curved surfaces using computation have been taken [21, 22, 23, 24] and algorithms have been suggested [25, 26, 27], the effect of surface curvature on MIPS has been investigated considerably less. Most studies focus either on polar particles [28, 29], ideal gas particles [30, 26], mixtures with passive particles [31] or on very specific cases of the phase space like very low or very high densities [32, 33, 34]. Additionally, most studies are limited primarily to spherical confinement, aside from a few exceptions [23, 24], and thus to systems with predominantly positive Gaussian curvature $K > 0$. The influence of confinement to exclusively negatively (saddle-like) curved surfaces $K < 0$ is unexplored even though such structures are ubiquitous in nature [35, 36, 37, 38, 39, 40].

In anticipation of the importance of curvature in synthetic active matter for applications such as colloidal robotics, we investigate the dynamic behavior of hard, non-polar SPPs on both positively and negatively curved surfaces. We performed molecular dynamics (MD) simulations of SPPs in spherical (positive Gaussian curvature) and hyperbolic (negative Gaussian curvature) space by confining them to sphere and gyroid minimal surfaces, respectively. While a sphere has constant positive Gaussian curvature, a surface of constant negative Gaussian curvature cannot be embedded in 3D Euclidean space without self-intersections or singularities. The gyroid, which has negative curvature everywhere, is the closest approximation of the hyperbolic plane in Euclidean space [41, 42]. We first investigate whether curvature shifts the critical density for the onset of MIPS, an important quantity in active matter studies, for low, intermediate and high curvature sphere and gyroid surfaces with regards to the particle size. We report an interesting geometrical lensing effect for surfaces of intermediate curvature, which we show theoretically arises from the nature of parallel lines in spherical and hyperbolic space. We next show that curvature destabilizes solid MIPS clusters, breaking them up into a dense fluid domain, which we relate to lattice defects dictated by the surface geometry. Finally, we synthesize our findings to give three examples of how simple, non-spherical confining surfaces may be designed to obtain novel MIPS phenomena. Specifically, we engineer *cyclic motility-induced phase separation* (CMIPS) on spherocylinders, where clusters of SPPs alternately assemble and disassemble (see Movie 1); *directionally biased cyclic motility-induced phase separation* (DBCMIPS) on "spherocones", where SPPs alternately assemble at one end and disassemble at the other (see Movie 2); and *positional cluster fluctuations* on metaballs where large, spatiotemporal fluctuations in cluster size and position occur (see Movie 3).

2. Simulation methods

In our molecular dynamics simulations we model the self-propelled particles (SPP) as spherical objects with diameter σ. The equations of motion are described by overdamped active Brownian dynamics confined to the different surfaces

$$\begin{aligned} \gamma\dot{\mathbf{r}}_i &= F_i^{\mathrm{Act}} + F_i^{\mathrm{Man}} + \sum_j \mathbf{F}_{ij}^{\mathrm{Ex}} \\ \dot{\theta}_i &= \sqrt{2D_r}\Lambda_{r,i}, \end{aligned} \tag{1}$$

with $\gamma = 1$ being the drag coefficient. We use a non-thermal model of SPPs to focus solely on the influence of geometry and to guarantee that all the reported effects indeed stem from the curvature of the underlying surfaces rather than other potential sources of origin like thermal fluctuations. The inter-particle force $\mathbf{F}_{ij}^{\mathrm{Ex}}$ is derived from the purely repulsive Weeks-Chandler-Anderson potential [43]

$$V^{\mathrm{ex}}(r_{ij}) = \begin{cases} 4\epsilon\left(\left(\frac{\sigma}{r_{ij}}\right)^{12} - \left(\frac{\sigma}{r_{ij}}\right)^{6}\right) - \epsilon & \text{if } r_{ij} < r_{\mathrm{cut}} \\ 0 & \text{else} \end{cases} \tag{2}$$

with $r_{\mathrm{cut}} = 2^{\frac{1}{6}}\sigma$ and energy unit $\epsilon = 1$. Note that we determine the distance of the particles as the Euclidean distance and not the geodesic distance based on the surface. The active force $F_i^{\mathrm{Act}} = v_0\hat{\mathbf{v}}_i(\theta_i)$ is given by a unit vector $\hat{\mathbf{v}}_i(\theta_i) = v_i(\hat{\mathbf{e}}_{t_1}(\mathbf{r}_i)\cos\theta_i + \hat{\mathbf{e}}_{t_2}(\mathbf{r}_i)\sin\theta_i)$ and the active force amplitude v_0. The unit vector $\hat{\mathbf{v}}_i$ describes the director of the active driving force in terms of the vectors $\hat{\mathbf{e}}_{t_1}(\mathbf{r}_i)$ and $\hat{\mathbf{e}}_{t_2}(\mathbf{r}_i)$, which span the local tangent plane of the confining surface at point $\mathbf{r}_i$. We indicate the ratio between rotational diffusion and active propulsion by the persistence length $l = \frac{v_0}{D_r} = 100\sigma$. As shown in Fig. SI1, all observed collective behavior is independent of l for $l > 50\sigma$. The rotational diffusion of the director is described by the rotational diffusion coefficient D_r and modeled as uniformly distributed white noise $\Lambda_{r,i}$ such that $\langle\Lambda_{r,i}\rangle = 0$ and $\langle\Lambda_{r,i}\Lambda_{r,j}\rangle = \delta_{ij}$. The force $F^{\mathrm{Man}} = \lambda\hat{\mathbf{n}}(\mathbf{r}_i)$ points in the normal direction $\hat{\mathbf{n}}(\mathbf{r}_i)$ of the confining surface to keep the SPPs attached to the manifolds. For the analytical form of the confining surfaces, see Appendix A. The magnitude λ is calculated by using a RATTLE algorithm [25]. The confinement to the manifold introduces the dimensionless parameter $\frac{R_c}{\sigma}$ based on the curvature radius R_c in addition to the reduced persistence length $\frac{l}{\sigma}$, the reduced energy parameter $\frac{\epsilon}{v_0^2}$ and the packing fraction ϕ.

The global packing fraction in a system of N particles is approximated by $\phi = \frac{N\pi(\sigma/2)^2}{A_{\mathrm{surf}}}$, where A_{surf} is the area of the surface to which the particles are confined. The surface of the flat 2D plane, the 2-sphere and the gyroid are identified as $A_{\mathrm{pl}} = L^2$, $A_{\mathrm{sph}} = 4\pi R_{\mathrm{c}}^2$ and $A_{\mathrm{gyr}} = 8A_0a^2$, respectively. The simulations were initialized by placing N passive particles on the surfaces with low curvature and low density. Afterwards, K was slowly increased until the desired density $\rho \in [0.08, 0.55]$ and curvature radius $R_c \in [1.4\sigma, 25\sigma]$ was reached. The exact values are indicated in the phase diagrams of

Fig. 1. In the next step, we activated the active forces and waited for $5 \cdot 10^7 \delta t$ with the time-steps $\delta t = 1 \cdot 10^{-3} \tau$ to guarantee a steady state. Lastly, we sampled the simulations for $5 \cdot 10^7 \delta t$. We performed all our simulations with the HOOMD-blue simulation toolkit (v2.9) [44] and measured time in units of $\tau = \frac{\sigma}{v_0}$. We analyzed the simulations with freud [45] and used the signac [46] software package for data management.

3. Results

3.1. Gaussian curvature shifts the onset of phase separation

To study MIPS in relation to the Gaussian curvature of the confining surface, we investigated the collective behavior of SPPs on spheres and gyroids with different mean curvature radii $R_c = \frac{1}{\sqrt{|K|}}$. Our findings are summarized in a phase diagram based on the observed clustering behavior (see Fig. 1 also for clustering definition). The phase diagrams were generated by gridding up the design space linearly within the density range $\phi = [0.08, 0.56]$ and logarithmically within the curvature range $|K| = [1.61 \cdot 10^{-3} \sigma^{-2}, 0.672 \sigma^{-2}]$ into a total of 700 points. As shown in the phase diagram, particle clustering directly depends on whether SPPs are confined to surfaces of low curvature, high curvature or intermediate curvature. SPPs on low-curvature spheres and gyroids behave as though they are confined to a plane as all studied surfaces are locally approximately flat. We observe this region for Gaussian curvatures below $|K| \lesssim 0.003 \sigma^{-2}$. The behavior of SPPs on surfaces of high and intermediate curvature is more interesting.

On highly curved surfaces with $|K| \gtrsim 0.02 \sigma^{-2}$, we determine that the collective behavior of the SPP systems is affected or even dominated by topological effects. These topological effects are different on the sphere than on the gyroid. On the sphere, MIPS is ill-defined because it is hardly possible to distinguish between fluctuations and clustering due to the small number of particles that can occupy the surface (see also Fig. 1a). However, the high degree of spatial confinement leads to a spontaneous swarming behavior where SPPs obtain the same great circle trajectories and align; the connection between this microswarming phenomenon and the confinement was reported and discussed in Ref. [33]. On the gyroid, however, the particles form amorphous networks with only 2-3 contacts per particle (see Fig. SI2 and Fig. 1b), a markedly different structure than the close packed hexagonal configurations observed in flat space. With hyperbolic (negative curvature) surfaces, the onset density for clustering is higher than in flat space because of the openness of the network-like domains. Note that the particles interact via an Euclidean metric rather than according to their geodesic distance. This means that in the high curvature regime SPPs do not interact close to the embedded surface – an approximation we make for the medium and low curvature regime – but their point of contact during a collision is instead located considerably inside the confining sphere

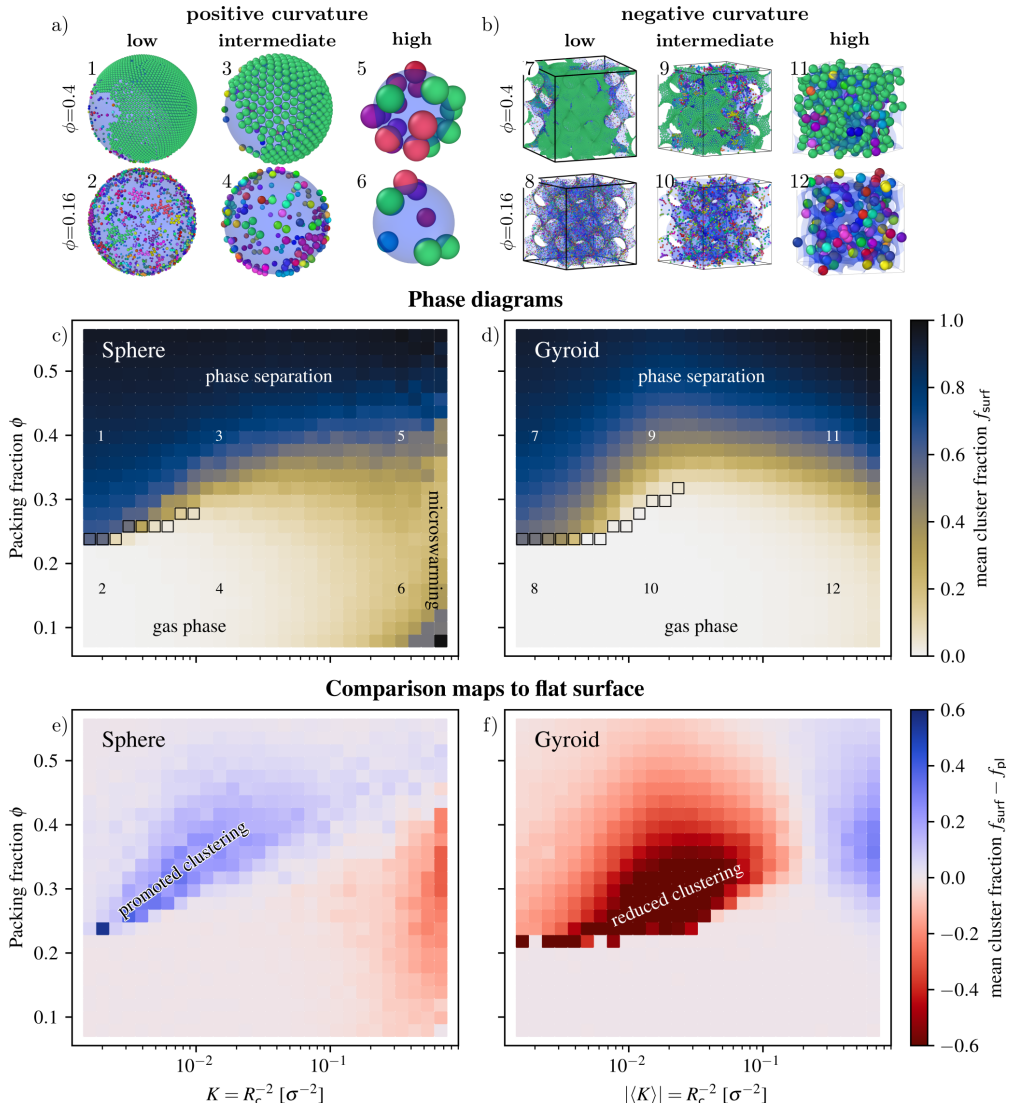

Figure 1. a+b): Snapshots from simulations of the sphere (a) and gyroid (b) systems in the high ($|K|$=0.34σ^{-2}) medium ($|K|$=0.015σ^{-2}) and low ($|K|$=0.002σ^{-2}), curvature regime at two densities ϕ=0.16 and ϕ=0.4 and persistence length $l = 100\sigma$. The particles are colored based on their cluster affiliation. For the cluster construction, two SPPs, i and j, are considered neighbors if they interact. The numbers indicate the position within the phase space of (c) and (d). c+d) Color map of the mean cluster fraction $f = \frac{1}{N}\sum_i^N \frac{m_i}{N}$ for SPPs on a sphere surface (c) or on a $2 \times 2 \times 2$ periodic gyroid (d) with the number of total particles N and the number of members m_i within the cluster of the i-th particle. The phase space is sampled based on the packing fraction ϕ and the mean curvature K. The black outlined squares indicate where metastable clusters form in the medium and high curvature regime (see Fig. SI3). e+f): Comparison color map between the weighted cluster fraction $\Delta f = f_{surf} - f_{pl}$ of (c)/(d) and of a corresponding system where the SPPs are confined to a flat plane with equal surface area $A_{pl} = A_{surf}$ as the sphere (e) and gyroid (f) surface, respectively. The comparison maps allow us to distinguish between finite-size and curvature effects. Here, blue/red areas indicate curvature regions with higher/lower mean cluster fraction than on their flat counterpart.

and inside the channel domains of the gyroid, respectively. This type of interaction effectively increases the geodesic size of the particles and enhances the topological effects.

Intermediate between the low and high curvature regime, we identify a region where topological effects can be mostly neglected, yet the systems respond to the local confining geometry in opposite ways for spherical and hyperbolic environments. Spherical confinement promotes phase separation and clustering at lower packing densities (see blue region in Fig. 1e) than in flat space, while the gyroid surface suppresses clustering and the dense phase forms at higher densities (see red region in Fig. 1f). This contrary effect is explained by the characteristics of spherical and hyperbolic geometry. We designed our simulations such that freely moving SPPs follow geodesic trajectories. In spherical geometry, geodesics correspond to great circles on the bounding sphere where parallel lines do not exist. The pathways of two particles that move in the same direction thus converge and eventually intersect. Consequently, positive curvature acts as a convex lens and increases the probability for SPPs to collide and cluster. In contrast, geodesic trajectories of SPPs traveling in the same direction on a hyperbolic surface are hyper-parallel and diverge from one another. Therefore, negative curvature acts as a concave lens to disperse the particles and suppress clustering.

In addition to the formation of a stable dense domain with a converging number of particles at high densities, we observe large fluctuations of the size of the largest cluster at the onset of phase separation in curved systems (see Fig. SI3). In this regime SPPs form clusters; however, the clusters disperse and collapse during the growth process. We explain this destabilization of large clusters by the enhanced motility of particles inside the dense domain (see section 3.2 for a more in-depth discussion). In combination with small total particle numbers (on the sphere) or the variance in Gaussian curvature (on the gyroid surface), increased internal motility leads to clusters breaking into smaller parts which then either dissolve or again grow into larger domains. As the fluctuations are not well captured by our clustering measures we define the onset of phase separation if growing clusters contain 25% of the total number of particles before collapsing (see black framed squares in Fig. 1)‡. We do not observe a similar phenomenon on flat surfaces.

To understand the different clustering behaviors on differently curved surfaces we theoretically predict the onset densities of clustering $\phi_o(K)$ based on the growth rate of seed clusters, which are precursors of phase separation. We use a minimal model similar to Ref. [47]. Consider a circular seed of radius r within a homogenous gas of SPPs with velocity vector $v_0\hat{\mathbf{v}}$. For seeds to grow into large clusters, the influx of SPPs from the gas phase must exceed the outflux of seed particles back into the gas. We express the evaporation rate by $k_{\text{out}}(K) = \kappa_{\text{out}} C(K)$ in terms of the seed circumference $C(K)$ since

‡ Note here that a different choice for the cut-off changes our results only marginally as the fluctuation amplitudes quickly increase.

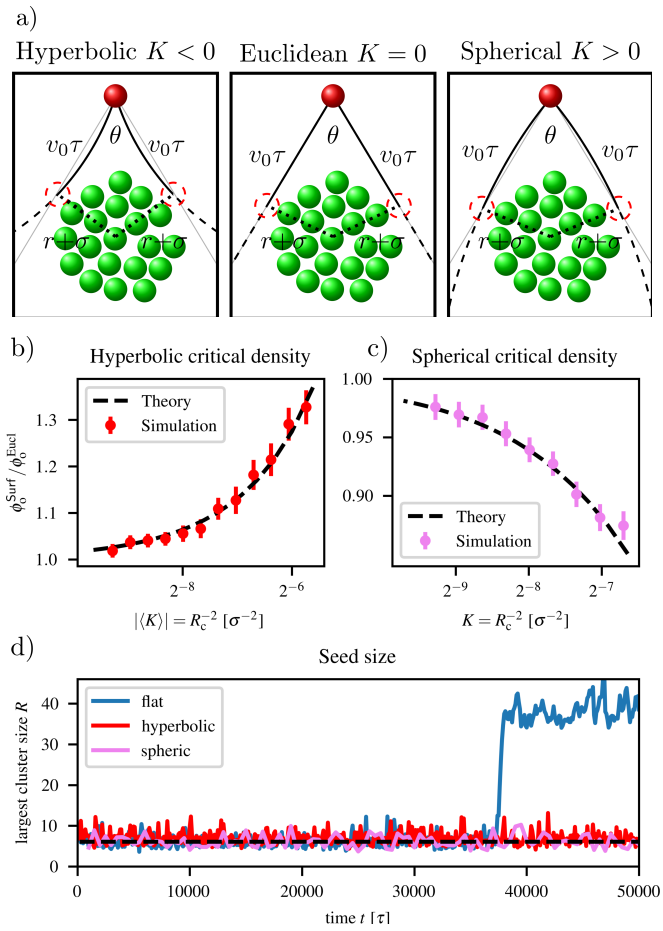

Figure 2. a) Schematic of the collision window of an SPP (red) with a circular seed cluster (green) in two-dimensional hyperbolic, Euclidean and spherical space from left to right. The collision angle θ of a particle at position x and velocity v_0 is derived from the maximal distance a SPP can travel per time τ and the radius of the cluster r. By increasing or decreasing Gaussian curvature $|K|$ the particle trajectories bend towards and away from the cluster, respectively. We use θ to calculate the collision probabilities in Eq. (5). b+c) The onset density for phase separation at $l = 100\sigma$ and different curvature K in the medium regime. The onset of clustering is measured on the gyroid (b) and the sphere (c) in relation to flat space and compared to the theoretical predictions of Eq. (7) with seed size $r = 6.4\sigma$ (c). d) Radius of the largest cluster during representative simulations in hyperbolic ($|\langle K \rangle| = 0.012\sigma^{-2}$, $\phi = 0.26$), spherical ($K = 0.012\sigma^{-2}$, $\phi = 0.26$) and flat space ($L_b = 282\sigma$, $\phi = 0.22$) at the onset density. We approximate the seed size as $\sqrt{2}r_g$ with the radius of gyration r_g. The seed size before clustering (dashed line) is of similar magnitude as the choice of r in b) and c).

only particles at the gas-seed interface can leave the cluster. The factor κ_{out} denotes the average loss rate of particles per unit length. We identify k_{out} in Euclidean, spherical and hyperbolic space as

$$\begin{aligned} k_{\text{out}}^{\text{Eucl}} &= 2\pi r \kappa_{\text{out}}, \\ k_{\text{out}}^{\text{Sph}}(K) &= 2\pi K^{-\frac{1}{2}} \sin\left(r\sqrt{K}\right) \kappa_{\text{out}}, \\ k_{\text{out}}^{\text{Hyp}}(K) &= 2\pi |K|^{-\frac{1}{2}} \sinh\left(r\sqrt{|K|}\right) \kappa_{\text{out}}. \end{aligned} \tag{3}$$

To derive the equation for the absorption rate $k_{\text{in}}(K)$, we must determine the number of particles that collide with the seed per time unit τ, within which an unimpeded SPP travels roughly a distance $v_0\tau$. Hence, only particles within the shell $r+\sigma \leq x \leq r+\sigma+v_0\tau$ must be taken into account. Since the direction of $\hat{\mathbf{v}}$ is uniformly distributed due to diffusion, a particle at a distance x from the center of the seed is on a collision course with the cluster if it moves within the collision cone with angle $\theta(K)$ (see Fig. 2a). By assuming that $r+\sigma > v_o\tau$, we can approximate θ by the law of cosines in Euclidean, spherical and hyperbolic trigonometry

$$\begin{aligned} (r+\sigma)^2 &= x^2 + (v_0\tau)^2 - 2x(v_0\tau)\cos\left(\frac{\theta^{\text{Eucl}}}{2}\right), \\ \cos((r+\sigma)\sqrt{K}) &= \cos(x\sqrt{K})\cos(v_0\tau\sqrt{K}) + \sin(x\sqrt{K})\sin(v_0\tau\sqrt{K})\cos\left(\frac{\theta^{\text{Sph}}}{2}\right), \\ \cosh((r+\sigma)\sqrt{K}) &= \cosh(x\sqrt{K})\cosh(v_0\tau\sqrt{K}) - \sinh(x\sqrt{K})\sinh(v_0\tau\sqrt{K})\cos\left(\frac{\theta^{\text{Hyp}}}{2}\right). \end{aligned} \tag{4}$$

Therefore, the collision probabilities $p(x) = \frac{\theta(x)}{2\pi}$ are given by

$$\begin{aligned} p^{\text{Eucl}}(x) &= \frac{\arccos\left(\frac{x^2+(v_0\tau)^2-(r+\sigma)^2}{2x(v_0\tau)}\right)}{\pi}, \\ p^{\text{Sph}}(x) &= \frac{\arccos\left(\frac{\cos((r+\sigma)\sqrt{K})-\cos(x\sqrt{K})\cdot\cos(v_0\tau\sqrt{K})}{\sin(x\sqrt{K})\cdot\sin(v_0\tau\sqrt{K})}\right)}{\pi}, \\ p^{\text{Hyp}}(x) &= \frac{\arccos\left(\frac{\cosh(x\sqrt{|K|})\cdot\cosh(v_0\tau\sqrt{|K|})-\cosh((r+\sigma)\sqrt{|K|})}{\sinh(x\sqrt{|K|})\cdot\sinh(v_0\tau\sqrt{|K|})}\right)}{\pi}. \end{aligned} \tag{5}$$

See Fig. 2a for a pictorial description of these equations. By integrating over the shell around the seed in the respective spaces and approximating that the gas density is roughly the same as the global density before the nucleus grows $\phi_g \approx \phi$, we can write:

$$\begin{aligned} k_{\text{in}}^{\text{Eucl}} &= \phi \int_0^{2\pi} \int_{r+\sigma}^{r+\sigma+v_0\cdot\tau} p^{\text{Eucl}}(x)\cdot x \mathrm{d}x = \phi \cdot P^{\text{Eucl}} \\ k_{\text{in}}^{\text{Sph}}(K) &= \phi \int_0^{2\pi} \int_{r+\sigma}^{r+\sigma+v_0\cdot\tau} p^{\text{Sph}}(x)\cdot \frac{\sin(x\sqrt{K})}{\sqrt{K}} \mathrm{d}x \\ &= \phi \cdot P^{\text{Sph}}(K) \\ k_{\text{in}}^{\text{Hyp}}(K) &= \phi \int_0^{2\pi} \int_{r+\sigma}^{r+\sigma+v_0\cdot\tau} p^{\text{Hyp}}(x)\cdot \frac{\sinh(x\sqrt{|K|})}{\sqrt{|K|}} \mathrm{d}x \\ &= \phi \cdot P^{\text{Hyp}}(K). \end{aligned} \tag{6}$$

If we assume that κ_{out} is equal in all three cases and if $k_{\text{in}}(K) = k_{\text{out}}(K)$ is in balance at the onset density ϕ_o, we can predict the shift of $\phi_o^{\text{Sph/Hyp}}$ on the sphere and the gyroid in relation to ϕ_o^{Eucl} in Euclidean space. By combining Eq. (3) and Eq. (6), we get:

$$\begin{aligned}\phi_o^{\text{Sph}}(K) &= \frac{k_{\text{out}}^{\text{Sph}}(K)}{k_{\text{out}}^{\text{Eucl}}} \frac{P^{\text{Eucl}}}{P^{\text{Sph}}(K)} \phi_o^{\text{Eucl}} \\ \phi_o^{\text{Hyp}}(K) &= \frac{k_{\text{out}}^{\text{Hyp}}(K)}{k_{\text{out}}^{\text{Eucl}}} \frac{P^{\text{Eucl}}}{P^{\text{Hyp}}(K)} \phi_o^{\text{Eucl}}.\end{aligned} \tag{7}$$

In Fig. 2(b-c) we fit both functions to our computational results and obtain good agreement between theory and simulation for the seed size $r = 6.4\sigma$. This size value coincides with the typical sizes of precursor clusters observed in simulations in both flat and curved 2D space at the onset density and before the system starts to phase separate (see Fig. 2(d)). Our theoretical approach also explains that dense clusters are not stable at the high negative curvature regions of the gyroid at the onset of phase separation. The resulting cluster size fluctuations are discussed further in section 3.3.

3.2. Curvature induces geometric fluidization of dense SPP clusters

In addition to the observed shifted phase separation, curvature also affects the dynamics within the cluster. In flat space, SPPs in the dense phase move within the hexagonally ordered lattice structure via dislocation diffusion [47]. However, clusters on both positively and negatively curved surfaces are more mobile than in flat space due to topologically mandated defect scars, which are known to also emerge in packings of hard particles on curved surfaces [48, 49]. Whereas particles inside a cluster still form crystalline patches separated by grain boundaries at low curvature, hexagonal order itself becomes less prominent by curving the underlying surface. The system then separates not into a gas and a solid phase but instead into a gas and a high density diffusive fluid phase of flowing particles (see Fig. 3). We call this mechanism, which is similar to grain boundary melting [50, 51, 52], *geometric fluidization* of the cluster. This fluid nature is present even in the active crystal limit where the dense phase spans the sphere or the gyroid.

To directly relate defects to particle motility and to show an increase of defect chains, that are known to drive the melting of clusters in active systems [53], we obtained the local density distribution based on Voronoi tessellation in flat and curved systems with $R_c = 8.2\sigma$. In Fig. 4 we use the inverse area of the Voronoi cells as an approximation of local density at different packing fractions. In the flat system the local density in the phase separated state is bimodal, which we attribute to the gas and the hexagonally ordered solid phase. Hence, SPPs within the cluster bulk are trapped by their six neighbors causing solid clusters with few internal rearrangements. In addition, the distributions on both the gyroid and the sphere indicate a bifurcated high density peak with two sub-domains. Peak I in Fig. 4 represents tightly packed particles

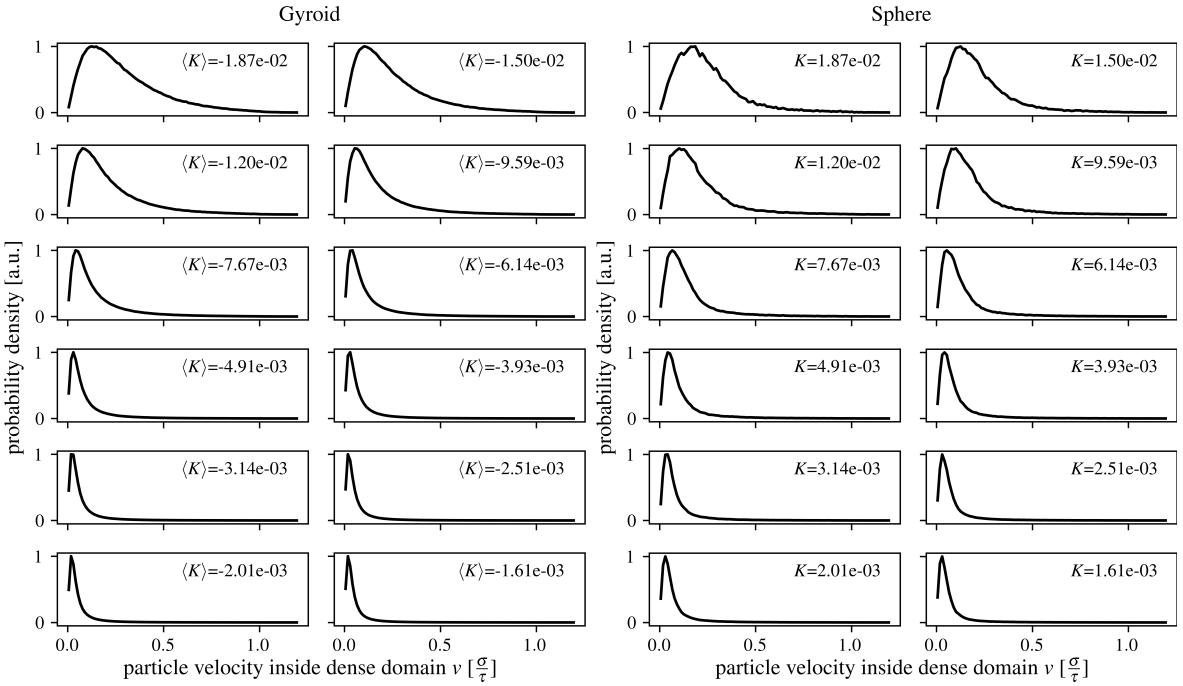

Figure 3. Velocity distribution of particles within the bulk of the dense cluster at packing fraction $\phi = 0.48$ and persistence length $l = 100\sigma$. The velocity of the particles is estimated by the distance Δd a particle travels within τ. The particles live on a $3 \times 3 \times 3$ periodic gyroid surface (left) or a sphere (right) with varying mean curvature K.

within a mostly hexagonal environment, while peak II, which is dominant at the onset of phase separation, arises from defect patterns; the topologically necessary defect scars. The average coordination number within the dense regions for highly curved surfaces in Fig. SI2 supports the conclusion that scar patterns dominate the system and all particles are affected by the geometry induced defects. The position of peak II is consistent with the density distribution in flat space, where, even though no secondary high-density peak occurs, the presence of defects and grain boundaries is suggested by a small bump. The second peak in the hyperbolic and spherical systems shrinks with density and, eventually, is indistinguishable from peak I. The importance of defect patterns for the fluidization of the clusters becomes even more apparent by relating local density with velocity. The motility of particles decreases with the density of their environments. Closely packed particles are practically arrested within the crystal besides the collective motion of the cluster. At local densities close to peak II we observe an increase in velocity in all three systems in accordance to other studies on flat surfaces [50, 51, 52, 53]. However, particles with a local density close to peak II are faster on the sphere and the gyroid than in flat space. Therefore, by introducing additional defect patterns that destabilize the balance of forces in their close vicinity, curvature enhances the mobility of particles, induces flow and eventually fluidizes the whole cluster.

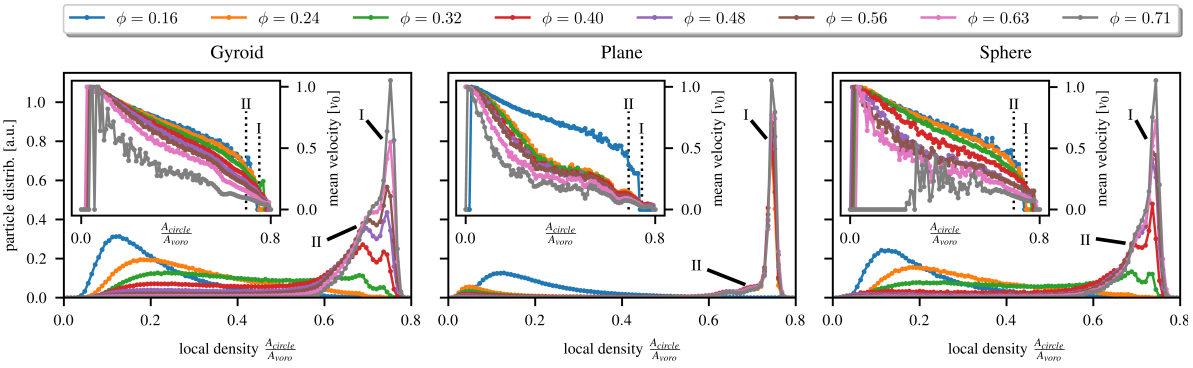

Figure 4. Local density distribution based on the Voronoi diagrams on the gyroid (left), plane (center) and sphere surface (right) at curvature radius $R_c = 8.2\sigma$ and different packing fractions. The peaks annotated with I and II indicate particles within a hexagonal environment and within defect patterns, respectively. The inset plots are the same local density distributions weighted by the mean translation per time step $v = \frac{\Delta d}{\tau}$.

3.3. Design and engineering of novel, curvature-induced non-equilibrium phenomena

Based on the above findings, we hypothesize that we can obtain new dynamic phenomena in SPP systems confined to closed surfaces that strategically combine regions of positive, negative and zero Gaussian curvature. Here we present three such examples, depicted in Fig. 5, where we spatially control both phase separation and cluster size fluctuations.

Cyclic motility-induced phase separation – Because cluster stability is different on surfaces of different curvature, we hypothesized that by combining positive and zero Gaussian curvatures in a closed surface we could induce cyclic motility-induced phase separation (CMIPS). A spherocylinder is one such surface, combining regions of positive Gaussian curvature (the spherical caps) and zero Gaussian curvature (the cylinder). We confined SPPs to a spherocylinder of length $L = 2\pi R$ and radius $R = 10\sigma$. The radius was chosen to produce enhanced phase separation at the caps with $K = 0.01\sigma^{-2}$ according to Fig. 1. As expected, we observe MIPS above $\phi > 0.25$, but the SPPs form clusters already at lower densities. In a narrow window $0.235 < \phi < 0.25$, the particle density is high enough to induce clustering at the positively curved caps, but low enough to both prevent clustering and destabilize dense regions on the cylindrical part where $K = 0$. The different cluster stabilities on different areas of the spherocylinder surface leads to a temporally cyclic phase-separated state as indicated by the cluster fraction and the particle density along the symmetry axis in Fig. 5d+g). From an isotropic phase, a cluster starts to grow at one of the spherical caps. This cluster moves away from the caps to the cylindrical part of the surface, where it is not stable and dissolves into the surrounding gas-like phase. These additional particles increase the density of the gas phase such that clusters can reform at the caps (see also Fig. 5a) and Movie 1), and the cycle repeats. Spectral analysis of the time-resolved cluster fraction indicates

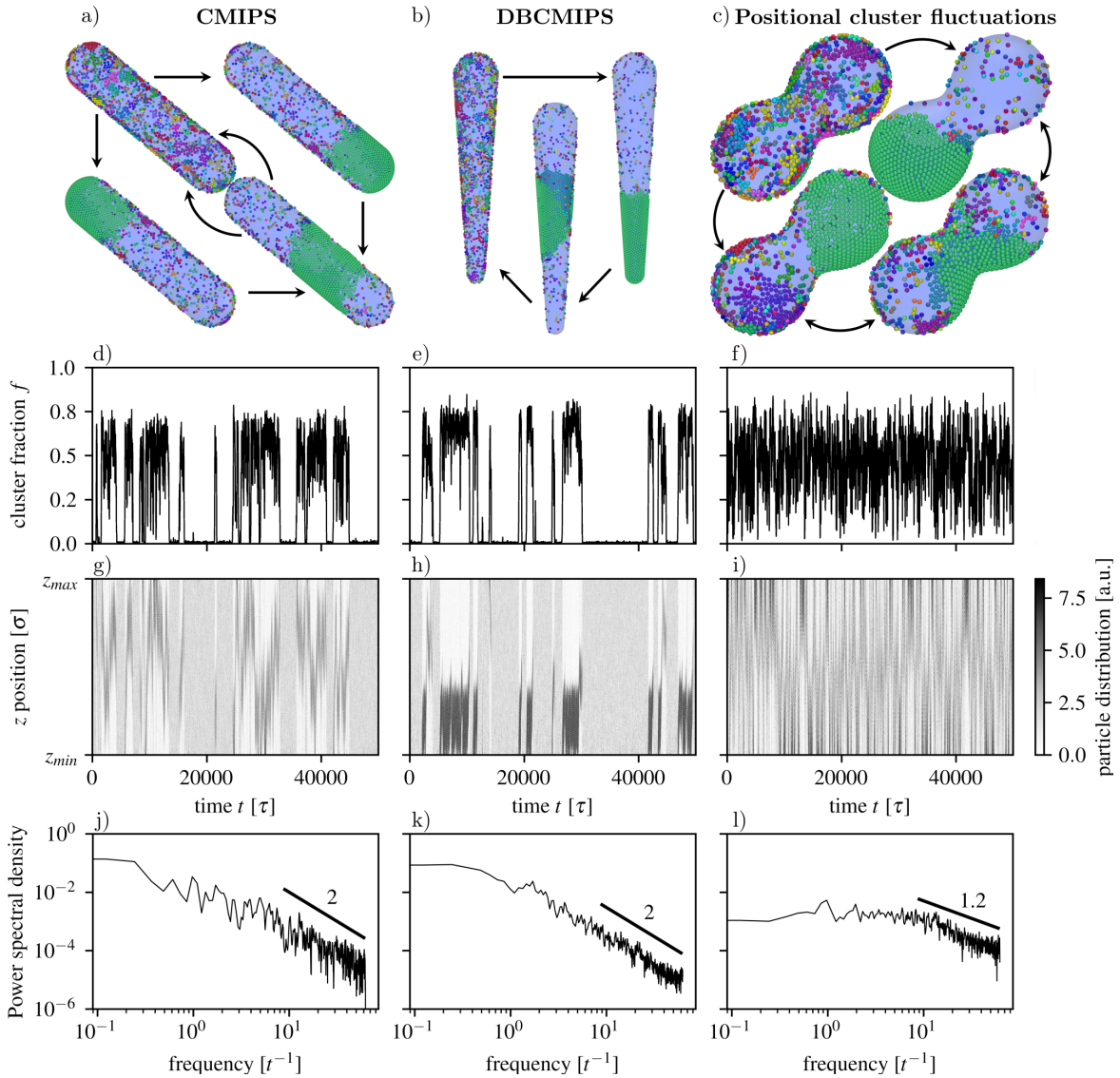

Figure 5. Top: Schematics of the three different curvature-induced non-equilibrium phenomena: a) cyclic motility-induced phase separation CMIPS (spherocylider), b) directionally biased cyclic motility-induced phase separation DBCMIPS (spherocone) and c) positional cluster fluctuations (metaball). The cluster fraction (upper center) and the local density (lower center) along the symmetry axis z during a representative simulation of active particles confined to a d+g) spherocylider ($R = 10\sigma$, $\phi = 0.24$; see Movie 1), e+h) spherocone ($R = 10\sigma$, $r = 4\sigma$, $\phi = 0.24$; see Movie 2) and f+i) metaball ($R = 9.5\sigma$, $L = 24\sigma$, $\phi = 0.28$; see Movie 3). Botom: Spectral analysis of the time-resolved cluster fractions of SPPs within j) the CMIPS, k) DBCMIPS and l) positional cluster fluctuation processes based on the corresponding cluster fraction profiles of d), e) and f). The power spectral densities of CMIPS and DBCMIPS are roughly inversely proportional to the squared frequency indicating red or $\frac{1}{f^2}$-noise. Yet, the positional cluster fluctuations resemble pink or $\frac{1}{f}$-noise more.

that the signal of CMIPS can be compared to red noise (see Fig. 5j). This indicates that the switch between phase separated and gas phase follows a random two state

Brownian process [54]. We observe CMIPS for spherocylinders with radius $R \leq 12\sigma$ ($K \geq 6.9 \cdot 10^{-3}\sigma^{-2}$). For larger radii, the cluster still develops on one of the end caps but no longer dissolves in the zero Gaussian curvature regions.

Directionally biased cyclic motility-induced phase separation – CMIPS can be engineered to create a directionally biased behavior where the cyclic phase separation is directed always from one side (see Fig. 5b). By decreasing the radius r of one of the caps while keeping the other radius R constant, a second, differently positively curved area on the surface is introduced. On this "spherocone" surface we again observe CMIPS, but the curvature asymmetry biases cluster formation towards the smaller cap as indicated in Fig. 5e+h) and Movie 2 with $R = 10\sigma$ and $r = 4\sigma$. After forming at the small cap ($K = 0.0625\sigma^{-2}$), the cluster travels towards the large cap into the flat region, dissolves and reforms at the small cap again. We call this phenomenon curvature-induced directionally biased cyclic motility-induced phase separation (DBCMIPS).

Positional cluster fluctuations – Combining surfaces of positive and negative Gaussian curvature provides another strategy for obtaining novel phases. Such a combination can be found in a metaball that comprises two spheres separated by a distance L such that the two spheres overlap to create a negatively curved "bridge" between them. In our simulations we confine SPPs to a metaball with sphere radii $R = 9.5\sigma$ and separation length $L = 24\sigma$. On the metaball surface we also detect CMIPS below a packing fraction of $\phi = 0.28$. Above this density, dense clusters of SPPs form predominantly on the positively curved spherical portions ($K = 0.011\sigma^{-2}$) and move into the negatively curved bridge connecting the two metaballs. In this hyperbolic region clusters shrink in size without dissolving completely. From the bridge the cluster then travels either back to one of the two spherical regions, where it grows again. This back and forth between growing and shrinking of the cluster results in high spatiotemporal variations of the cluster fraction, as shown in the temporarily high local density at the ends of the metaball and the generally lower local density at the center of the metaball in Fig. 5c+f+i) and Movie 2. In contrast, the fluctuations in spherical confinement are spatially invariant. Spectral analysis suggests that the fluctuations of the cluster fraction exhibit a frequency scaling behavior reminiscent of pink rather than red noise (see Fig. 5l). Pink or flickering noise is typical for bistable stochastic processes [54, 55] and ubiquitous in biological and physical systems [56].

4. Conclusion

In this paper, we studied the effect of negative and positive Gaussian curvature on the motility-induced phase separation of active self-propelled particles. We first introduced curvature by confining the particles to a sphere or gyroid minimal surface. In both cases we identified topological and geometrical effects that alter the onset of phase separation.

In the medium curvature regime we showed computationally and predicted analytically the promotion and inhibition of phase separation based on a geometric lensing effect. We explain this geometric lensing on the sphere and gyroid surface by the transition from Euclidean geometry to spherical and hyperbolic geometry, respectively. At high curvature we observed two different dominant topological effects. On positive curvature we reproduced the spontaneous microswarming reported in Ref. [33], which prevents the formation of dense clusters. On negative curvature the particles are more likely to form clusters based on a change in connectivity. Moreover, we investigated the transition from solid to fluid clusters by introducing curvature. We showed that curving the underlying surface is a mechanism to incorporate geometrically induced defect patterns, which locally melt the active crystal.

Based on these results we managed to design four new non-equilibrium phases. Due to the different onset of clustering in different regions of the surfaces we triggered cyclic phase separation on a spherocylinder, cluster waves on a spherocone, cluster fluctuations on a metaball surface and positional clustering around a sinusoidal peak. In general our findings considerably broaden the understanding of the effect of curvature on the steady states of self-propelled particle systems. In particular, the combination between fluidization and the mutable onset of phase separation suggests curvature being a promising tool to control active particle systems for colloidal robotic applications without requiring highly complex particle interactions [57, 58]. For instance, CMIPS on the spherocylinder and spherocone implies possible applications in particle transport where SPPs aggregate around a load within a positively curved environment, transport it and release it by dispersing due to negative curvature. Overall curvature navigation can be seen as an intrinsically driven alternative to colloidal swarm control via external stimuli [59, 60, 61, 62, 63] and potentially brings us closer to a particle swarm-based version of curvotaxis [64].

Acknowledgements

The authors thank Corwin Kerr, Sophie Youjung Lee and Gabrielle Jones for helpful discussions. This work was supported as part of the Center for Bio-Inspired Energy Science, an Energy Frontier Research Center funded by the U.S. Department of Energy, Office of Science, Basic Energy Sciences under Award # DE-SC0000989. The work was conceived with support from a grant from the Simons Foundation (256297, SCG). This work used the Extreme Science and Engineering Discovery Environment (XSEDE), which is supported by National Science Foundation grant number ACI-1548562; XSEDE award DMR 140129. Computational resources and services were also supported by Advanced Research Computing at the University of Michigan, Ann Arbor.

Appendix A. Curvature and confinement

To study phase separation at different curvature profiles, we confine the positions of all particles $\mathbf{r}_i = (x, y, z)^T$ to either (I) spheres with radius R_c (positive Gaussian curvature $K = \frac{1}{R_c^2} > 0$)

$$0 = x^2 + y^2 + z^2 - R_c^2, \tag{A.1}$$

(II) gyroid minimal surfaces with unit cell length a and surface frequency $\omega = \frac{2\pi}{a}$ (negative Gaussian curvature $K = -\frac{1}{R_c^2} < 0$)

$$0 = \sin(\omega x)\cos(\omega y) + \sin(\omega y)\cos(\omega z) + \sin(\omega z)\cos(\omega x) \tag{A.2}$$

or (III) the two-dimensional flat plane ($K = 0$). In the negative curvature simulations the unit cell length $a = \frac{L_b}{2}$ is coupled to the simulation box with size L_b such that it matches the periodicity of the surface and always contains 8 unit cells of the gyroid in a 2×2×2 arrangement unless specifically mentioned otherwise. We keep a constant unit cell number to compare between different Gaussian curvatures consistently. The next largest symmetric composition of unit cells 3×3×3 more than triples the number of particles within a simulation and is, hence, computationally too demanding for low curvature systems. Spot tests do not show any qualitative and only minor quantitative differences between simulations on the 2×2×2 and 3×3×3 gyroid surface in the medium and low curvature regime. As K is not constant throughout the gyroid surface, we define the curvature radius in terms of the mean Gaussian curvature: $R_c = \sqrt{-\langle K \rangle^{-1}}$. The linear relation between a and R_c is derived from the Gauss-Bonnet theorem $R_c = \sqrt{-\frac{A_0}{2\pi\chi}}a \approx 0.3508a$ [65], where $\chi = -2$ is the Euler characteristic and $A_0 a^2 = 3.092124a^2$ is the surface area of the gyroid per unit cell [41].

For the simulations on the three exemplary surfaces, which feature the three novel phase separated states, we restricted the positions of all particles to a spherocylinder (cyclic phase separation)

$$0 = \begin{cases} x^2 + y^2 + (z - \frac{L}{2})^2 - R^2 & \text{if } z > \frac{L}{2} \\ x^2 + y^2 + (z + \frac{L}{2})^2 - R^2 & \text{if } z < -\frac{L}{2} \\ x^2 + y^2 - R^2 & \text{else} \end{cases} \tag{A.3}$$

with radius R and length L, a spherocone (cluster waves)

$$0 = \begin{cases} x^2 + y^2 + (z - \frac{L}{2})^2 - r^2 & \text{if } z > \frac{L}{2} + r\frac{R-r}{L} \\ x^2 + y^2 + (z + \frac{L}{2})^2 - R^2 & \text{if } z < -\frac{L}{2} + R\frac{R-r}{L} \\ x^2 + y^2 - \left(\frac{(r-R)z + \frac{L}{2}(r+R)}{\sqrt{L^2 - (R-r)^2}}\right)^2 & \text{else,} \end{cases} \tag{A.4}$$

with two differently sized spherical cap with radii r and R and length L, a metaball surface (cluster fluctuations)

$$0 = \frac{1}{x^2 + y^2 + (z - \frac{L}{2})^2} + \frac{1}{x^2 + y^2 + (z + \frac{L}{2})^2} - \frac{1}{R^2} \tag{A.5}$$

with radius R and distance L between the two metaballs and a sinusoidal peak (positional clustering)

$$0 = \begin{cases} h\cos\left(\frac{2\pi}{L}\sqrt{(x^2+y^2)}\right)^2 - z & \text{if } \sqrt{(x^2+y^2)} < \frac{L}{4} \\ z & \text{else} \end{cases} \tag{A.6}$$

with periodicity length L and height h.

[1] Hemelrijk CK, Hildenbrandt H. Schools of fish and flocks of birds: their shape and internal structure by self-organization. Interface focus. 2012;2(6):726–737.

[2] Pearce DJG, Miller AM, Rowlands G, Turner MS. Role of projection in the control of bird flocks. Proc Natl Acad Sci USA. 2014;111(29):10422–10426.

[3] Ito S, Uchida N. Emergence of a giant rotating cluster of fish in three dimensions by local interactions. arXiv preprint arXiv:210605892. 2021;.

[4] Subramanian G, Koch DL. Critical bacterial concentration for the onset of collective swimming. J Fluid Mech. 2009;632:359.

[5] Be'er A, Ilkanaiv B, Gross R, Kearns DB, Heidenreich S, Bär M, et al. A phase diagram for bacterial swarming. Commun Phys. 2020;3(1):1–8.

[6] Prost J, Jülicher F, Joanny JF. Active gel physics. Nat Phys. 2015;11(2):111–117.

[7] Gangwal S, Cayre OJ, Bazant MZ, Velev OD. Induced-charge electrophoresis of metallodielectric particles. Phys Rev Lett. 2008;100(5):058302.

[8] Walther A, Muller AHE. Janus particles: synthesis, self-assembly, physical properties, and applications. Chem Rev. 2013;113(7):5194–5261.

[9] Brown A, Poon W. Ionic effects in self-propelled Pt-coated Janus swimmers. Soft Matter. 2014;10(22):4016–4027.

[10] Das D, Lauga E. Active particles powered by Quincke rotation in a bulk fluid. Phys Rev Lett. 2019;122(19):194503.

[11] Arslanova A, Dugyala VR, Reichel EK, Reddy N, Fransaer J, Clasen C. 'Sweeping rods': cargo transport by self-propelled bimetallic microrods moving perpendicular to their long axis. Soft Matter. 2021;17(9):2369–2373.

[12] Wensink HH, Löwen H. Emergent states in dense systems of active rods: from swarming to turbulence. J Phys Condens Matter. 2012;24(46):464130.

[13] Mandal R, Bhuyan PJ, Chaudhuri P, Rao M, Dasgupta C. Glassy swirls of active dumbbells. Phys Rev E. 2017;96(4):042605.

[14] Bonilla LL, Trenado C. Contrarian compulsions produce exotic time-dependent flocking of active particles. Phys Rev E. 2019;99(1):012612.

[15] Cates ME, Tailleur J. Motility-induced phase separation. Annu Rev Condens Matter Phys. 2015;6(1):219–244.

[16] Marchetti MC, Fily Y, Henkes S, Patch A, Yllanes D. Minimal model of active colloids highlights the role of mechanical interactions in controlling the emergent behavior of active matter. Curr Opin Colloid Interface Sci. 2016;21:34–43.

[17] Turci F, Wilding NB. Phase separation and multibody effects in three-dimensional active Brownian particles. Phys Rev Lett. 2021;126(3):038002.

[18] Keller R. Cell migration during gastrulation. Curr Opin Cell Biol. 2005;17(5):533–541.

[19] Krndija D, El Marjou F, Guirao B, Richon S, Leroy O, Bellaiche Y, et al. Active cell migration is critical for steady-state epithelial turnover in the gut. Science. 2019;365(6454):705–710.

[20] Lin SZ, Li Y, Ji J, Li B, Feng XQ. Collective dynamics of coherent motile cells on curved surfaces. Soft Matter. 2020;16(12):2941–2952.

[21] Sknepnek R, Henkes S. Active swarms on a sphere. Phys Rev E. 2015;91(2):022306.

[22] Apaza L, Sandoval M. Brownian self-driven particles on the surface of a sphere. Phys Rev E. 2017;96(2):022606.

[23] Ai BQ, Zhu WJ, Liao JJ. Collective transport of polar active particles on the surface of a corrugated tube. New J Phys. 2019;21(9):093041.
[24] Hindes J, Edwards V, Kamimoto S, Stantchev G, Schwartz IB. Stability of milling patterns in self-propelled swarms on surfaces. Phys Rev E. 2020;102(2):022212.
[25] Paquay S, Kusters R. A method for molecular dynamics on curved surfaces. Biophys J. 2016;110(6):1226–1233.
[26] Apaza L, Sandoval M. Active matter on Riemannian manifolds. Soft Matter. 2018;14(48):9928–9936.
[27] Yang Y, Li B. A simulation algorithm for Brownian dynamics on complex curved surfaces. J Chem Phys. 2019;151(16):164901.
[28] Vicsek T, Czirók A, Ben-Jacob E, Cohen I, Shochet O. Novel type of phase transition in a system of self-driven particles. Phys Rev Lett. 1995;75(6):1226.
[29] Shankar S, Bowick MJ, Marchetti MC. Topological sound and flocking on curved surfaces. Phys Rev X. 2017;7(3):031039.
[30] Fily Y, Baskaran A, Hagan MF. Active particles on curved surfaces. arXiv preprint arXiv:160100324. 2016;.
[31] Ai BQ, Zhou BY, Zhang XM. Binary mixtures of active and passive particles on a sphere. Soft Matter. 2020;16(20):4710–4717.
[32] Janssen LMC, Kaiser A, Löwen H. Aging and rejuvenation of active matter under topological constraints. Sci Rep. 2017;7(1):1–13.
[33] Bruss IR, Glotzer SC. Curvature-induced microswarming. Soft Matter. 2017;13(30):5117–5121.
[34] Praetorius S, Voigt A, Wittkowski R, Löwen H. Active crystals on a sphere. Phys Rev E. 2018;97(5):052615.
[35] Larsson M, Terasaki O, Larsson K. A solid state transition in the tetragonal lipid bilayer structure at the lung alveolar surface. Solid State Sci. 2003;5(1):109–114.
[36] Selstam E, Schelin J, Williams WP, Brain APR. Structural organisation of prolamellar bodies (PLB) isolated from Zea mays. Parallel TEM, SAXS and absorption spectra measurements on samples subjected to freeze–thaw, reduced pH and high-salt perturbation. Biochim Biophys Acta, Biomembr. 2007;1768(9):2235–2245.
[37] Almsherqi ZA, Landh T, Kohlwein SD, Deng Y. Cubic membranes: the missing dimension of cell membrane organization. Int Rev Cell Mol Biol. 2009;274:275–342.
[38] Wilts BD, Leertouwer HL, Stavenga DG. Imaging scatterometry and microspectrophotometry of lycaenid butterfly wing scales with perforated multilayers. J R Soc Interface. 2009;6(suppl_2):S185–S192.
[39] Han L, Che S. An overview of materials with triply periodic minimal surfaces and related geometry: from biological structures to self-assembled systems. Adv Mater. 2018;30(17):1705708.
[40] Saranathan V, Narayanan S, Sandy A, Dufresne ER, Prum RO. Evolution of single gyroid photonic crystals in bird feathers. Proc Natl Acad Sci USA. 2021;118(23).
[41] Schröder GE, Ramsden SJ, Christy AG, Hyde ST. Medial surfaces of hyperbolic structures. Eur Phys J B. 2003;35(4):551–564.
[42] Schröder-Turk GE, Fogden A, Hyde ST. Bicontinuous geometries and molecular self-assembly: comparison of local curvature and global packing variations in genus-three cubic, tetragonal and rhombohedral surfaces. Eur Phys J B. 2006;54(4):509–524.
[43] Weeks JD, Chandler D, Andersen HC. Role of repulsive forces in determining the equilibrium structure of simple liquids. J Chem Phys. 1971;54(12):5237–5247.
[44] Anderson JA, Glaser J, Glotzer SC. HOOMD-blue: A Python package for high-performance molecular dynamics and hard particle Monte Carlo simulations. Comput Mater Sci. 2020;173:109363.
[45] Ramasubramani V, Dice BD, Harper ES, Spellings MP, Anderson JA, Glotzer SC. freud: A software suite for high throughput analysis of particle simulation data. Comput Phys Commun. 2020;254:107275.

[46] Adorf CS, Dodd PM, Ramasubramani V, Glotzer SC. Simple data and workflow management with the signac framework. Comput Mater Sci. 2018;146:220–229.
[47] Redner GS, Hagan MF, Baskaran A. Structure and dynamics of a phase-separating active colloidal fluid. Phys Rev Lett. 2013;110(5):055701.
[48] Burke CJ, Mbanga BL, Wei Z, Spicer PT, Atherton TJ. The role of curvature anisotropy in the ordering of spheres on an ellipsoid. Soft Matter. 2015;11(29):5872–5882.
[49] Guerra RE, Kelleher CP, Hollingsworth AD, Chaikin PM. Freezing on a sphere. Nature. 2018;554(7692):346–350.
[50] Saito Y. Melting of dislocation vector systems in two dimensions. Phys Rev Lett. 1982;48(16):1114.
[51] Chui ST. Grain-boundary theory of melting in two dimensions. Phys Rev B. 1983;28(1):178.
[52] Deutschländer S, Boitard C, Maret G, Keim P. Grain-boundary-induced melting in quenched polycrystalline monolayers. Phys Rev E. 2015;92(6):060302.
[53] Digregorio P, Levis D, Cugliandolo LF, Gonnella G, Pagonabarraga I. Unified analysis of topological defects in 2D systems of active and passive disks. Soft Matter. 2022;18(3):566–591.
[54] Hänggi P, Jung P. Colored noise in dynamical systems. Adv Chem Phys. 1995;89(239-326):1.
[55] Eliazar I, Klafter J. A unified and universal explanation for Lévy laws and 1/f noises. Proc Natl Acad Sci USA. 2009;106(30):12251–12254.
[56] Szendro P, Vincze G, Szasz A. Pink-noise behaviour of biosystems. Euro Biophys J. 2001;30(3):227–231.
[57] Rubenstein M, Cornejo A, Nagpal R. Programmable self-assembly in a thousand-robot swarm. Science. 2014;345(6198):795–799.
[58] Yang Y, Bevan MA. Cargo capture and transport by colloidal swarms. Sci Adv. 2020;6(4):eaay7679.
[59] Palacci J, Sacanna S, Steinberg AP, Pine DJ, Chaikin PM. Living crystals of light-activated colloidal surfers. Science. 2013;339(6122):936–940.
[60] Zhang J, Guo J, Mou F, Guan J. Light-controlled swarming and assembly of colloidal particles. Micromachines. 2018;9(2):88.
[61] Yigit B, Alapan Y, Sitti M. Programmable Collective Behavior in Dynamically Self-Assembled Mobile Microrobotic Swarms. Adv Sci. 2019;6(6):1801837.
[62] Yang L, Zhang L. Motion Control in Magnetic Microrobotics: From Individual and Multiple Robots to Swarms. Annu Rev Control Robot Auton Syst. 2020;4.
[63] Chen M, Lin Z, Xuan M, Lin X, Yang M, Dai L, et al. Programmable dynamic shapes with a swarm of light-powered colloidal motors. Angew Chem. 2021;.
[64] Pieuchot L, Marteau J, Guignandon A, Dos Santos T, Brigaud I, Chauvy PF, et al. Curvotaxis directs cell migration through cell-scale curvature landscapes. Nat Commun. 2018;9(1):1–13.
[65] Allendoerfer CB. The Euler number of a Riemann manifold. Am J Math. 1940;62(1):243–248.